

## Frequency resolved interferometric detection of local density fluctuations in flames

Johannes Peterleithner, Florian Salcher, Jakob Woisetschläger\*

Institute for Thermal Turbomachinery and Machine Dynamics, Graz University of Technology

\* correspondent author: jakob.woisetschlaeger@tugraz.at

---

**Abstract** Low NO<sub>x</sub> strategies usually include lean combustion in order to reduce the flame temperature. Under certain conditions, this interaction can occur periodically as thermo-acoustic coupling, a reason why new premix combustion systems tend to have oscillations. Ongoing developments have pushed the sensitivity for density fluctuation measurements using laser vibrometers. In this experiment a variable geometry burner was enclosed in a liner, with the flame optically accessible through four fused silica windows. By this burner with adjustable flame conditions the cavity of the atmospheric model combustion chamber was excitable at a frequency around 200Hz. Resonant and non-resonant flame conditions were investigated and compared by laser vibrometer interferometry, schlieren visualization and OH\*/CH\* chemiluminescence.

---

### 1. Introduction

New emission-restrictions have added lean combustion to the industries development priorities. Lean combustion is capable of significantly reducing one of the most important emissions, which is NO<sub>x</sub>. This reduction is achieved by lowering the overall combustion temperature. Unfortunately, lean combustion is inherently less stable, and therefore more sensitive to changing parameters in the combustor.

Lean combustion is influenced by fluctuations of heat release, which again interacts with pressure variations. Under certain conditions, this interaction can occur periodically as thermo-acoustic coupling, a reason why new lean-premix combustion systems tend to have oscillations. One of the most common coupling effects starts with a fluctuating combustion which excites the cavity oscillation of the combustor. This standing wave varies the burner inlet conditions, thus varying the flow into the combustion region which again varies the heat release rate. All together results in an amplification of oscillation.

Efforts have been made in order to understand and model instabilities (e.g. Lieuwen and Yang, 2005). However, the effect has still not been fully understood, therefore oscillations cannot completely be avoided in the design process. The current approach is to adapt engines after they have been built. Simultaneously, active and passive control mechanisms have been developed to approach the problem. Passive systems employing acoustic dampers only decrease the amplitude of certain frequencies, while active systems are more flexible but also increase the grade of complexity (Dowling and Morgans, 2005; Dowling, 1995). Despite these problems, lean combustion is state of the art (Lechner and Seume, 2010).

Thermo-acoustic phenomenon are also problematic at partload and while changing the flow field. As a consequence, the combustion process faces either lean flame blow out or the flame attaches to the injector tip and increases the structure's temperature. The situation can be avoided by either turning off several burners and keeping the remaining ones turned on full load, or by employing variable geometry burners such as the one investigated in this paper. The former solution has the disadvantage of a non-uniform circumferential temperature profile hitting the first turbine stage, while the latter can maintain a homogeneous distribution. The variable geometry burner being the test object in this report has been first characterized in an earlier publication (Giuliani et al., 2012).

Recently, laser-vibrometers were used at Graz University of Technology to investigate thermo-acoustic flame oscillations. Such laser vibrometers consist of a Mach-Zehnder interferometer and are widely used to detect surface vibrations from machinery. With the help of an acoustic-optical modulator these interferometers record vibration velocity rather than surface amplitude providing a spectral signal increased by a factor of  $2\pi f$ , with  $f$  the frequency of the oscillation. Here, these systems are used to detect density fluctuations along the laser beam rather than geometrical changes in the optical path. These density fluctuations can be related to heat release and pressure fluctuations by

$$\frac{\partial \rho}{\partial t} = \frac{1}{c^2} \frac{\partial p}{\partial t} - \frac{\gamma - 1}{c^2} q_v \quad (1)$$

where  $c$  denotes the specific heat ratio,  $p$  the pressure,  $\rho$  the density and  $q_v$  the fluctuating component of the heat release rate per unit volume. In a flame and under atmospheric conditions the heat release term (second term on the right side) surpasses the pressure term, while outside the flame the heat release contribution can be neglected. A first proof of concept for combustion was published in Köberl et al., 2010 and Leitgeb et al., 2013. This technique was also compared to frequency modulated Doppler global velocimetry in Fischer et al., 2013 – a technique capable of extremely fast velocity measurements.

In this experiment presented herein, a the variable geometry burner was enclosed in a liner, with the flame optically accessible through four fused silica windows. This atmospheric model combustion chamber was excitable at a frequency around 200Hz. Resonant and non-resonant flame conditions were investigated and compared by laser vibrometer interferometry, schlieren visualization and OH\* / CH\* luminescence.

## 2. Combustor

In order to facilitate the laser-optical investigation of thermo-acoustic oscillations, a variable geometry premixed Methane/air burner was combined with in an optically accessible liner at atmospheric pressure. In such a burner an actuator alters a geometric parameter. This work and previous work (Peterleithner et al., 2013; Fischer et al., 2013; Giuliani et al., 2012) used a variable nozzle geometry to alter the flame in terms of rotation or swirl of the fluid and the exit area ratio of the exit nozzle. With such a concept all parameters of the flame can be set continuously and independently during operation. The rich-lean variable geometry burner is seen in Fig.1a with the most important parts colored in blue, yellow and turquoise. Throughout all tests the burner was operated vertically. The center body (Fig.1a, blue colored) is moveable in axial direction, varies the exit area with a  $D=4\text{mm}$  cone on top and thus the momentum, while the swirl strength is set by the ratio between axial and tangential air, while keeping the overall air- and Methane-flows constant. So, the flame can be altered from a center-body-anchored flame to a swirl stabilized one. By means of a stratifier (Fig.1a, white colored part) the axial air flow is forced into a purely axial direction.

During all investigations Methane was used as a fuel and was premixed with the tangential air in a mixing chamber in the outer bushing (Fig.1a, yellow and orange colored). While in the previous investigations four tangential bores provided the tangential gas mixture, here 8 tangential holes in four rows were used to inject the tangential air-Methane mixture (Fig.1a, orange colored part). This alteration in the design guaranteed a cylinder symmetric flame for the investigations presented, while in the previous design a structure of four clearly visible flames are seen. Additional cooling air was provided through a settling chamber mounted underneath a perforated metal plate (Fig.1a, turquoise colored; hole diameter 5mm, hole distance 5mm). This air served a coolant for the glass plates in the liner. In the previous work by Giuliani et al. (2012) all details on control and fuel supply including the metering and remote control is presented.

This previously performed characterization of the variable geometry burner without liner (Giuliani et al. 2012) showed that burner axial velocities are in the range of 2-6m/s, tangential velocities are at 1.5m/s and temperature rises up to 1200K. The investigations were done using stereoscopic PIV and Raman/Rayleigh scattering. An example is plotted in Fig.2.

The variable geometry combustor was placed in a liner of quadratic shape with a 140x140mm cross-section, 580mm length and four fused-silica windows, size 220x90mm. The lower edges of these windows were aligned with the exit plane of the nozzle, so that all the flame was observable. Different hoods of different size were tested, but we finally decided to use a hood with a 80mm circular opening. With a liner length of 580mm, a hood with 80mm exit bore and a rotational symmetric combustor a strong thermo-acoustic coupling occurred at about 200Hz. Around this test rig a 3x3x2.5m<sup>3</sup> box with two layers of sound absorbing curtains and a sound absorbing ceiling was assembled. The curtains were impregnated heat-resistant. To test cavity resonance in the liner, a full range speaker (FR 8 - 8  $\Omega$ , Visaton, Germany) was used to excite acoustic waves in the liner.

To observe such a ‘combustion chamber resonance’ we used an axial air flow of 0.61g/s, a tangential air flow of 0.54g/s, a Methane flow of 0.0739g/s and a cooling air flow of 0.96g/s. This resulted in a mass ratio between tangential and axial flow of 0.89 and an equivalence ratio  $\phi=1.1$  for the resonant condition. The equivalence ratio  $\phi$  is used to discuss the combustion in the primary zone and is the ratio of the actual oxygen-fuel ratio and the stoichiometric oxygen-fuel ratio, with lean mixtures  $<1$ . The characteristic for the burner operated with liner is shown in Fig.3. For all measurements the center body was moved 1mm upwards (in

flow direction, positive x axis). Four operation points with different mass flow rates and equivalence ratios are discussed in Fig.3. The numbers for these operation points are given in brackets, with the equivalence number first, the mass flow rates (tangential to axial air) second. In some areas of this characteristic a hysteresis is observed. Depending whether the mass ratio is decreased or increased the flame stays attached or lifted. This area is dashed in Fig. 3.

For the resonant condition (1.1/0.89) the model combustor is swirl stabilized. This concepts is also used in turbomachinery, eases ignition and stabilizes operation. Such a pre-mixed combustion forms a recirculation zone, bringing hot gas back into the flame region where it helps to ignite the fresh fuel-air mixture from the injector. The swirl or vortex breakdown drives this recirculation. At the vortex axis an internal stagnation point does form where the reverse flow establishes (Leibovich 1978). Centrifugal instabilities and Kelvin–Helmholtz instabilities can be found in this region as well (Wang et al. 2005). Such swirl stabilized flames are highly turbulent, making predictions difficult. To ease understanding of combustion instabilities and thermo-acoustic effects, local and time-resolved information of state variables is necessary.

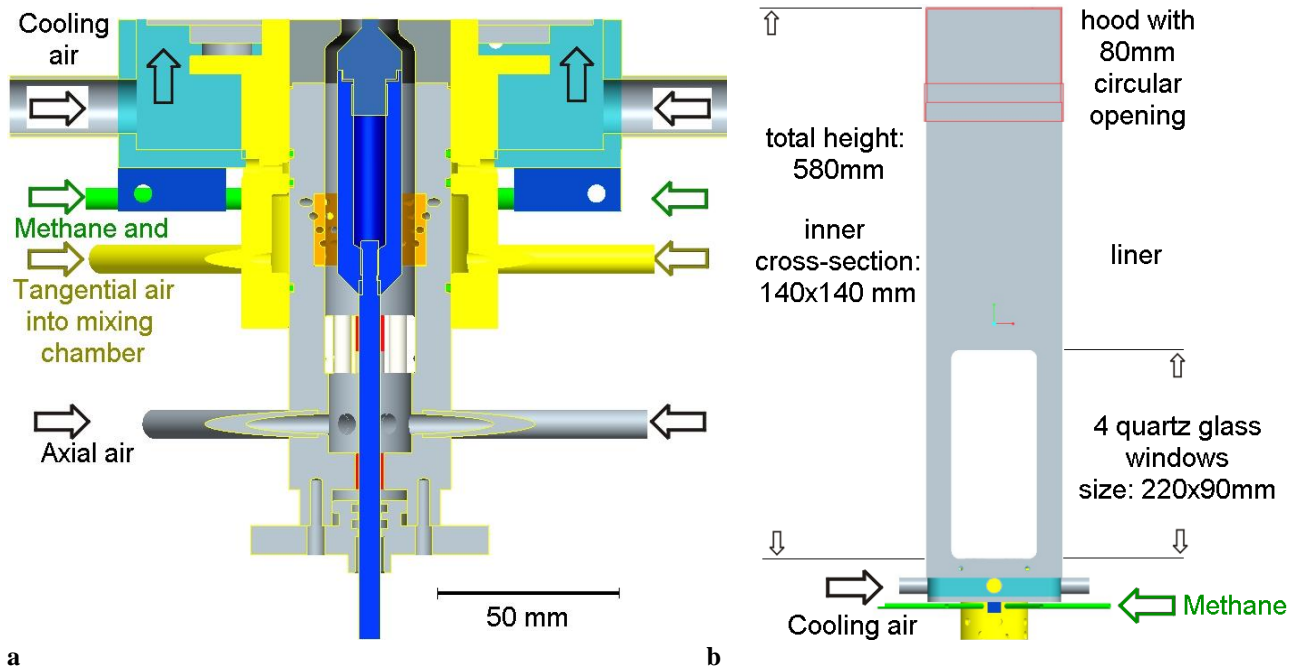


**Fig. 1 a)** Concept of the variable geometry combustor. Methane and tangential air are mixed in a chamber. Axial air is fed from below. The cooling air is supplied through a settling chamber underneath a perforated grid. **b)** combustion chamber, 580 mm height. The lower window edges match the exit bore of the nozzle. A suction blower was mounted app. 700mm above the orifice of the hood.

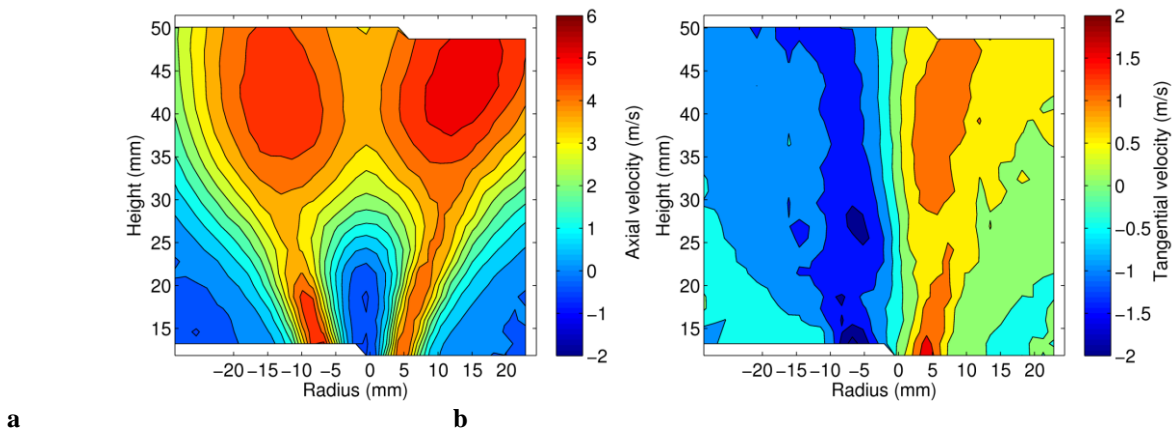


**Fig. 2 a)** axial and **b)** tangential velocities at local temperature up to 1200K at a mass flow rate of 0.44 and equivalence ratio  $\phi$  equal 1.4 (cone position 0mm). The recordings were done for a previous study without liner (Giuliani et al. 2012, Fischer et al. 2013).

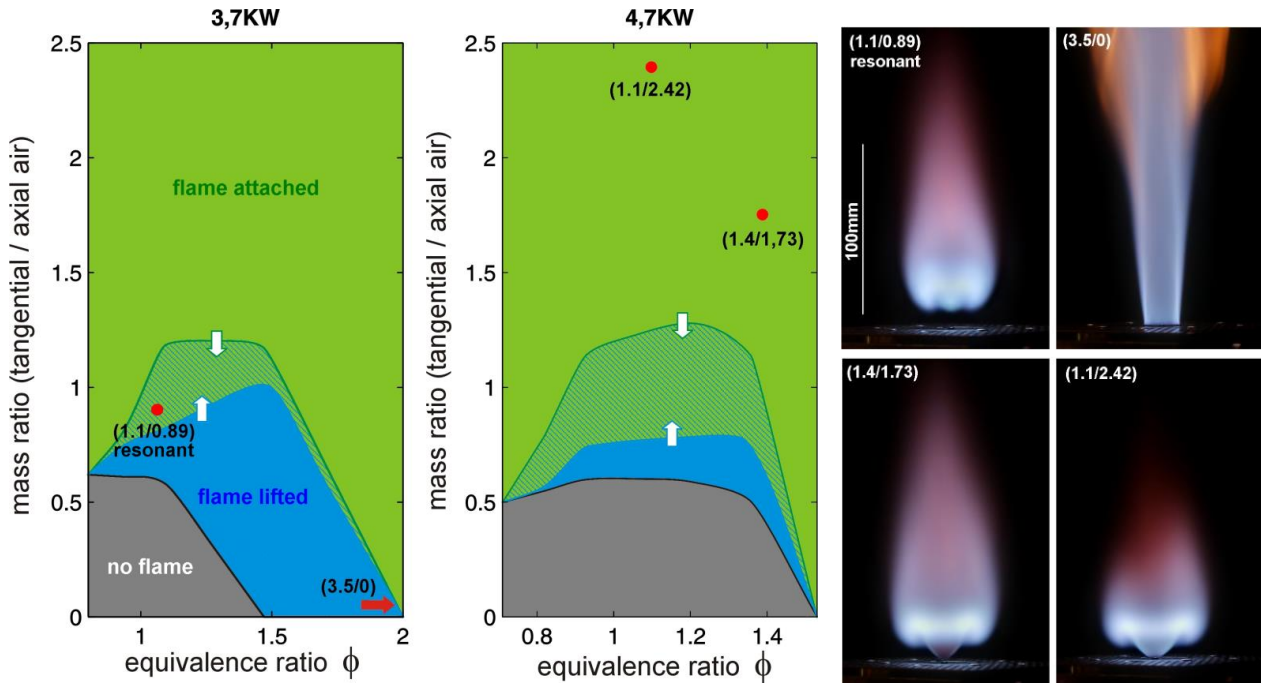


**Fig. 3** Variable geometry combustor characteristic for 3.7 kW and 4.7 kW. Cone position was +1mm (upwards direction, positive x axis). In the dashed area the flame is either attached (when the mass ratio is decreased during operation) or lifted (when the mass ratio is increased starting from a lifted flame). For four operation points the flame shape is shown to demonstrate the capability of the variable geometry burner.

### 3. Optical measurement techniques and visualization

#### 3.1 Interferometry - laser vibrometer

Laser vibrometer are widely used to detect surface vibrations of machinery. Basically they consist of a Mach-Zehnder interferometer with one arm leaving the device and the second one serving as reference arm. In this reference arm an acousto-optical modulator (Bragg cell) is placed, shifting the light frequency and causing a beating frequency (carrier frequency) at the vibrometer exit. After reflection from a surface the wave from the object arm is again superimposed with the reference wave inside the vibrometer device. The Doppler shifted wave reflected from the vibrating object surface now modulates the carrier frequency. Frequency demodulation helps to detect the surface velocity precisely. Based on this Doppler shift detection, such a system records the surface velocity rather than the vibration amplitude (Lewin 1999).

In return, at constant geometrical path a change in refractive index  $n(x,y,z,t)$  or the related density fluctuation in flow and combustion processes can be detected. In order to record density fluctuations the vibrating surface must be replaced by a rigidly fixed mirror (see Fig.4). The change in optical path length  $L$  is now given by

$$L = \int_z n(z,t) dz \quad , \quad (2a)$$

with  $z$  the laser beam direction. A factor 2 from passing the flame section twice is already considered. The integral indicates that this interferometric technique is line-of-sight measurement, integrating all index or density fluctuations along the beam path. Relating refractive index with local density  $\rho(x,y,z,t)$  can be done using the Gladstone-Dale relation

$$n - 1 = G \rho \quad , \quad (2b)$$

with the Gladstone-Dale constant  $G$  for the gas mixture. For the phase shift  $\varphi(t)$  between reference and object wave (and thus the optical path difference  $\Delta L$ ) we find

$$\varphi(t) = \frac{2\pi}{\lambda} \Delta L(t) = \frac{2\pi}{\lambda} G \int_z \Delta \rho(z,t) dz \quad . \quad (3)$$

This phase shift is now related to the output voltage from the vibrometer (with velocity decoder) by

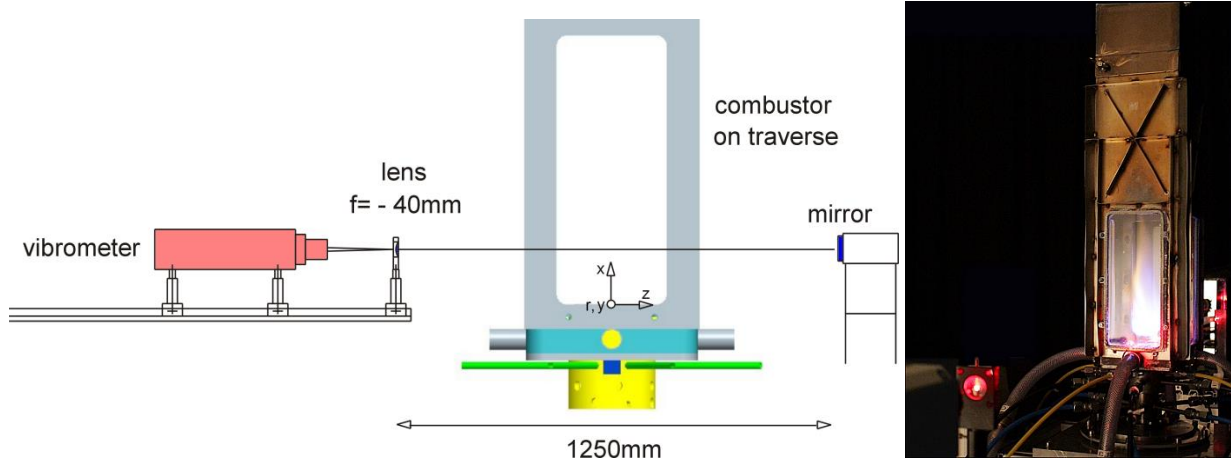


**Fig. 4** Setup for recording density fluctuations and the corresponding frequency spectra. The beam of the laser vibrometer is collimated by a -40mm lens. The mirror is rigidly mounted. The combustor is placed on a traverse, while the laser is fixed. The coordinate system is located in the nozzle center of the burner. z axis is beam direction.

$$\frac{\partial}{\partial t} \varphi(t) = \frac{2\pi}{\lambda} \frac{\partial}{\partial t} \Delta L(t) = \frac{2\pi}{\lambda} k_{vib} U(t) \quad (4)$$

$k_{vib}$  is the calibration constant of the vibrometer, here 5mm/s/V.  $U(t)$  is the vibrometer output voltage.

The application of velocity decoders give a better signal-to-noise ratio especially at higher frequencies, which gives an advantage against classical interferometry. For data recorded in this velocity mode, the output voltage is proportional to the time derivative of density fluctuations along the beam path. Splitting density into a time averaged mean and a fluctuating component according to the notations used in fluid mechanics we obtain

$$\frac{\partial}{\partial t} \rho(t) = \frac{\partial}{\partial t} (\bar{\rho} + \rho'(t)) = \frac{\partial}{\partial t} \rho'(t) \quad \left( = \frac{\partial}{\partial t} \Delta \rho(t) \right) \quad (5)$$

When recording frequency spectra or power spectra  $S(f)$  by a Fast-Fourier-Transform FT the time derivative of density fluctuations along the beam path can be transformed into the density fluctuation by using the  $2\pi f$  conversion factor at the given frequencies  $f$ :

$$S(f) = FT^2 \left[ \int \rho'(t) dz \right] = \frac{1}{4\pi^2 f^2} FT^2 \left[ \int \frac{\partial \rho'}{\partial t}(t) dz \right] = \frac{1}{4\pi^2 f^2} FT^2 \left[ \frac{k_{vib} U(t)}{G} \right] \quad (6)$$

After calculation of power and amplitude spectra the resultant number is a RMS value. To obtain the amplitude at a given frequency a factor of  $\sqrt{2}$  must be considered. This was done for all results presented in the next sections.

According to eqs.1, 3 and 4 the laser vibrometer now records fluctuations in pressure (sound waves) as well as fluctuations in heat release. In the flame the heat release term in eq.1 surpasses the pressure term, while outside the flame the heat release contribution can be neglected. Between these two contributions from inside (mainly heat release) and outside the flame (mainly pressure waves) a phase shift between density fluctuation signals from both sides of the flame front can be observed at certain frequencies, with such phase shifts depending on resonant conditions (Rayleigh criterion).

Finally local data of density fluctuations are advantageous. Since interferometric techniques do integrate along the line of sight, tomographic reconstruction of heat release related density fluctuations inside the flame at certain frequencies is a possibility to obtain local data. In case of rotational symmetry of the flame, a single projection can be used for tomographic reconstruction or Abel inversion. Here, we use the software package IDEA 1.7.31, developed at Graz University of Technology (Hipp et al., 1999; Hipp et al., 2004), <http://optics.tugraz.at/>.

Especially in a confined environment the use of tomographic reconstruction techniques for interferometric data is troubled by the so-called zero-fringe problem. For a good tomographic reconstruction the recorded numbers have to be zero at the boundary of each projection. Otherwise an unknown offset throughout the

reconstructed field will occur. This problem is not severe for an unconfined flame due to the relatively low density fluctuations (sound wave) in the far field, but might render measurements impossible in a combustion chamber with thermo-acoustic oscillations due to the strong sound pressure throughout the field. To avoid such uncertainty two laser vibrometers can be used together with a correlation technique for data reconstruction allowing the direct measurement of local density fluctuations even if the field of view is limited. This dual-laser-vibrometer technique was successfully applied to an isothermal circular free jet flow (Hampel and Woisetschläger, 2006) and a Methane flame (Köberl et al., 2010). When two laser beams intersect at angles of 90° within an interrogation area the cross-correlation  $C(f)$  can be calculated from the two laser vibrometer frequency spectra  $F_1(f)$  and  $F_2(f)$ :

$$\overline{C(f)} = \overline{F_1(f) \cdot F_2^*(f)} \quad (7)$$

Due to the turbulent nature of combustion and turbomachinery flows a high number of single spectra must be averaged to obtain meaningful results. The correlation spectra (power spectra) must be weighted by the size  $l$  of the interrogation area, which is function of mean velocity  $u$  and frequency  $f$ . For most cases this area function  $A(f)$  can be represented by

$$A(f) = l^2 = \left(\frac{u}{f}\right)^2 \quad (8)$$

In fields with strong pressure waves (sound fields) density fluctuations might occur in both beams simultaneously, not only in the interrogation area. The data validation procedure makes special use of the fact that in the intersection point of the laser beams the phase lag  $\Delta\Phi$  between both signals for a given frequency must be close to zero for local fluctuations in this point. A special filter function is defined by

$$|C_F(x, y, z, f)| = |C(x, y, f)| \cdot \exp\left[-\left(\frac{\Phi(x, y, z, f)}{\Delta\Phi(f)}\right)^2\right] \quad (9)$$

With  $x, y, z$  the position scanned. In order to avoid artifacts (e.g. by multiples of  $2\pi$ ) multidirectional scans might be advisable, meaning longer scanning times and stable flames.

The use of laser vibrometers proves to be useful for the investigation of unsteady flows (Woisetschläger et al., 2003a; Woisetschläger et al., 2003b; Mayrhofer et al., 2000), periodic flows (Mayrhofer and Woisetschläger 2001), and combustors (Leitgeb et al., 2013; Peterleithner et al., 2013; Fischer et al., 2013; Giuliani et al., 2012; Köberl et al., 2010; Giuliani et al., 2010). This technique is also used by other authors to investigate sound fields (Martarelli et al., 2013; Zipser and Franke, 2008; Harland et al., 2007; Gren et al., 2005; Buick et al., 2004; Harland et al., 2003; Zipser et al. 2002)

For most of the measurements a single laser vibrometer was used (interferometer head OFV-353, velocity decoder OFV-3001, calibration factor 5mm/s/V, calibration certificate 17.02.2014, 20kHz bandwidth, no filters, Polytec, Waldbronn, Germany). The second laser vibrometer needed for dual laser vibrometry was identical to the first. -40mm lenses were used to collimate the beam to 1.5-2mm diameter. To scan the field, the combustor was mounted on a DANTEC lightweight traverse (DANTEC Dynamics, Roskilde, Denmark), while the vibrometer was fixed. Data acquisition was performed with analog input modules NI-91215 (National Instruments, Austin, Texas) and Labview 8.6 software. For each position scanned 245760 samples were taken with a sample rate of 4096S/s. Together with the vibrometer voltage a microphone signal was recorded in position  $x=-140\text{mm}$ ,  $y=150\text{mm}$ ,  $z=150\text{mm}$  (KECG2738PBJ-A, miniature electret condenser microphone, omni-directional, -40dB, 2.8mm diameter, Kingstate Electronics Corp, New Taipei City, Taiwan). All cross-correlations and Fourier transforms were done by a Matlab routine using a sample length of 2048, providing frequency spectra (power, amplitude and phase) for each position scanned.

### 3.2 Chemiluminescence

Light emission measurements through the emission of  $\text{CH}^*$  or  $\text{OH}^*$  radicals in hydrocarbonate flames is a common technique to gain information about the flame shape, the heat release and the equivalence ration. In lean flames  $\text{CH}^*$  emission is observed giving the flame a blue hue, while in rich flames a greenish color indicates  $\text{C}_2^*$  emission. Soot particles will emit red or yellow light corresponding to Planck law.  $\text{OH}^*$  emits UV radiation.

Chemoluminescent emission recording is an established technique to indicate heat release and equivalence ratio in natural-gas-fuelled, premixed flames operating at atmospheric pressure. Hardalupas and Orain (2004) state that the intensity ratio of OH\*/CH\* emission decreases monotonically with the equivalence ratio for lean and stoichiometric mixtures, with uncertainties of 5% up to  $\phi = 1.1$  and 20% for rich flames. On the other hand the authors use CH\* and OH\* emissions as indicators for local, temporally resolved rates of heat release. This research by Hardalupas and Orain (2004) was performed for equivalence ratios between 0.7 and 1.3 and strain rates between 40 and 800s<sup>-1</sup>. Nori and Seitzman (2009) find that the OH\*/CH\* ratio is useful for recording equivalence ratio in lean premixed methane-air systems, but the relationship between CH\* chemiluminescence and heat release varies with equivalence ratio, pressure, temperature and strain. Only at high pressure the dependence on  $\phi$  and strain is found to be small. Lauer and Sattelmayer (2010) point out that integral measures of chemiluminescence can be used to monitor integral heat release rates of turbulent flames but no reliable information can be obtained for spatially resolved heat release rates. Panoutsos et al. (2009) find that strain rates have an effect on OH\* and CH\* chemiluminescence, but the OH\*/CH\* ratio is a monotonic function of equivalence ratio without effects from strain rate. The authors also mention that OH\*/CH\* ratio can help to distinguish between premixed and non-premixed reactions in turbulent flames. Finally Hardalupas (2010) present a chemiluminescence sensor for local heat-release rate and equivalence ratio measurements in a model gas turbine combustor. Panoutsos et al. (2009) and Guyot et al. (2010) give the relation between OH\*/CH\* ratio and equivalence ratio.

In this work OH\* and CH\* line-of-sight time-averaged chemiluminescence was recorded to estimate flame shape and local equivalence ratios. For this purpose a TECHSPEC Bandpassfilter 310nm was used for the OH\* emission (310±3nm CWL, FWHM 10±2nm Bandwidth, 50mm Mounted Diameter, 18% Transmission, Edmund Optics, Barrington, NJ, USA) and a TECHSPEC Bandpassfilter 430nm for the CH\* emission (430±2nm CWL, FWHM 10±2nm Bandwidth, 50mm Mounted Diameter, 98% Transmission, Edmund Optics, Barrington, NJ, USA). To record line-of-sight time averaged chemoluminescence images at 430nm a CCD-camera was deployed (DMK 31BF03, monochrome progressive scan, IEEE 1394, 1024 x 768 pixel, Imaging Source, Maisach, Germany) together with a TV lens (12.5-75mm, f/1.8, TOKINA, Tokyo, Japan). An ICCD camera recorded and measured at 430nm and 310nm (NanoStar, 1280x1024pixel, Photocathode radiant sensitivity 310nm/430nm = 65%, DaVis 7.6 Software, LaVision, Göttingen, Germany) together with a UV lens (UV, 105mm, f/4.5, Nikon, Tokyo, Japan). Both systems were carefully calibrated using neutral density filters for visible (MGA, Melles Griot Inc., CA, USA) and UV ( fused silica NDUV, UV Metallic ND, Thorlabs, NJ, USA). A background image was always recorded. To calculate local values from integral line-of-sight measurements tomographic reconstruction algorithms were used, even when the flame proved to be symmetric when rotated around the x-axis and only one projection was needed for reconstruction. The tomographic convolution scheme for back-projection was preferred against an Abel inversion due to less noise generation in the center of the reconstructed field (Pretzler et al., 1992). Details on the tomographic reconstruction software IDEA 1.7.31 <http://optics.tugraz.at/> can be found in Hipp et al. (1999).

### 3.3 Schlieren visualization

Flow visualization was done by schlieren technique (Settles, 2006). The liner was placed between two f=2032mm, 280mm diameter parabolic mirrors, with 2.7m distance between the mirrors. A halogen lamp illuminated a 1mm aperture, the light beam then expanded, was folded by a plane elliptical mirror, collimated by the parabolic mirror, transilluminated the test rig, focused by the second parabolic mirror, folded again and entered a 1mm schlieren stop (dark field schlieren technique). 700 frames were recorded with a 3CCD camera (NV-DX100EG, Panasonic, Osaka, Japan) at full aperture, 1/8000s, 0dB. For each sub-image only the 10% brightest pixels were used in an image averaging process. This procedure produces bright traces which show small, turbulent structures as well as streamlines around the combustion zone. The turning traces of these streamlines indicate the swirling nature of the flame in this line-of-sight visualization technique.

## 4. Results and discussion

### 4.1 Validation of rotational flame symmetry around x axis

To validate the rotational symmetry of the variable geometry burner, all together 18 images (projections) at 10 degrees intervals were recorded using the spectral emittance at 430nm (CH\* filter) and the IEEE 1394 CCD camera, while rotating the burner without liner around its x axis. Operating conditions were  $\phi = 1.1$  at

mass ratio 0.89. Total exposure time per projection was 8s at  $f/2.4$ , gain 5. Rotational center alignment, length calibration and intensity calibration using the neutral density filters were performed. The tomographic reconstruction was done using a convolution technique in IDEA 1.7.31 software with 54 projections, linearly interpolated from the 18 projections recorded. This interpolation was done to suppress star-like artifacts during reconstruction. From local intensities in different radial directions, one can estimate the rotational symmetry to be within 10%. In Fig.5 the projections in observation direction (z-axis) is shown together with the upper part of the variable geometry burner, on the right side are tomographic reconstructions of four planes perpendicular to the flame axis (x-axis). The planes are labeled from A – D.

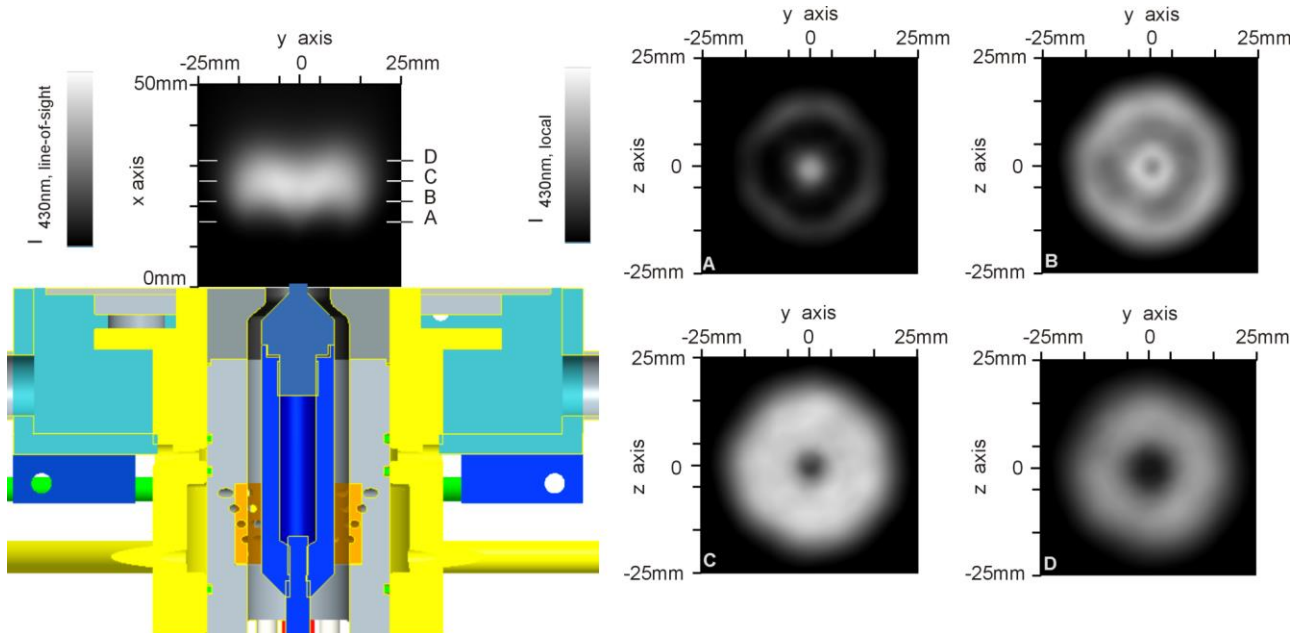


**Fig. 5** Tomographic reconstruction of the flame shape from the spectral emittance  $I$  at 430nm ( $\text{CH}^*$ ) for  $\phi = 1.1$  at mass ratio 0.89 ('resonant' flame). The flame was unconfined. 18 projections were recorded to verify the rotational symmetry which is within 10% with respect to the local intensity values in section C. Left is a single projection perpendicular to the observation direction (z-axis) together with the burner, right are four reconstructed planes perpendicular to the flame axis x. The planes are labeled from A–D.

#### 4.2 Structural vibrations and cavity resonance

In turbomachinery flows, density fluctuations from vortex shedding or blade passing are in the range of 7kHz to 40kHz, with higher harmonics contributing to the signal. In combustors relevant frequencies caused by flow or combustion oscillations are much lower and might overlap with structural vibrations. Therefore great care has to be taken already during design and construction of the test rig and the experimental setup. Setup vibrations must be tested by hitting single parts in the setup (mirror, laser vibrometer, rail system, traverse) while recording the spectrum. To record liner vibrations the laser vibrometer directly hit the surface while the surface was mechanically excited and spectra were recorded. Optimization of the liner was done in iterations by welding reinforcement plates on the liner until the frequency range relevant for chamber or flame oscillations was free of vibrational resonance frequencies. Fig.6 shows the result with the low frequency bending modes of the liner, the high frequency line plate vibrations (above 300Hz) and the setup vibrations. In order to reduce setup vibrations in the signal, the lens and the liner glass plates were slightly tilted by less than 1degree to avoid direct reflections into the vibrometer receiving optics.

From the voltage amplitude  $U_0(f)$  recorded by the laser vibrometer the vibration amplitude  $\Delta L$  for a given frequency  $f$  can be calculated by

$$\Delta L(f) = \frac{k U_0(f)}{2 \pi f} \quad , \quad (10)$$

with  $k$  the calibration factor of the system (0.005m/s) which gives oscillation amplitudes of 0.3 $\mu$ m in Fig.6. This amplitude depends on the strength of mechanical excitation.

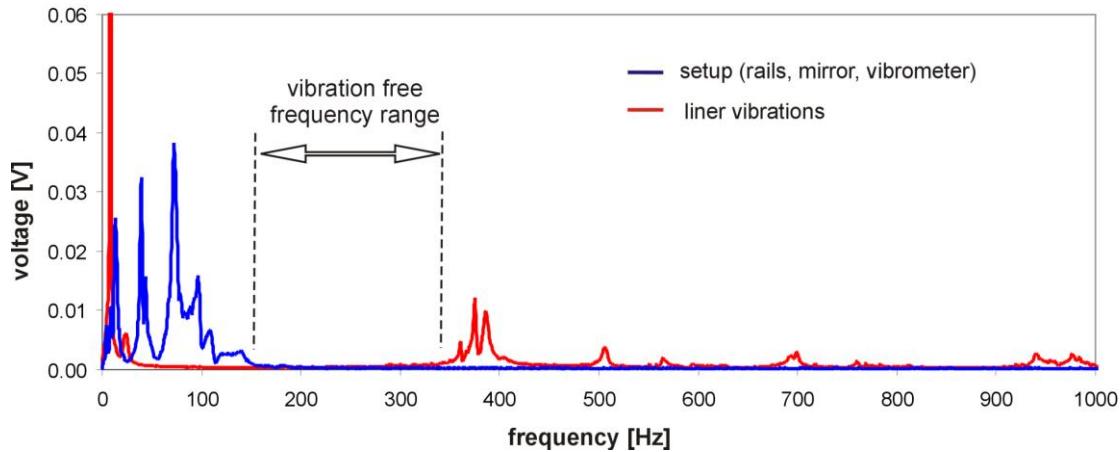


**Fig. 6** Structural vibrations in the experimental setup. On the one side there are possible vibrations by the setup (mirror, laser vibrometer, rail system, traverse) on the other side the surface of the liner might also vibrate at plate resonance frequencies.

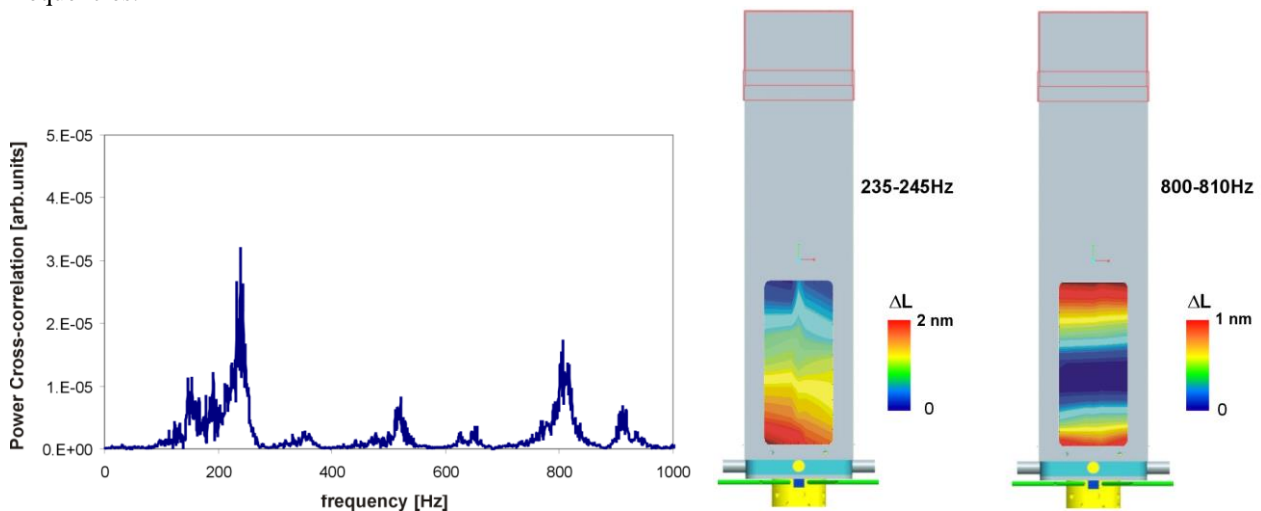


**Fig. 7** Acoustic cavity resonances in the liner without flame. Shown is the cross-spectrum between the signal from the laser vibrometer in position  $x=180\text{mm}$  and  $y=0\text{mm}$ , with a pronounced resonance 230-250Hz. For two resonance frequencies the vibrometer was scanned trough the field to plot the mode shape.

At constant geometrical path,  $\Delta L$  represents the line-of-sight change in refractive index  $n(x,y,z,t)$  or density  $\rho(x,y,z,t)$  and can be used to detect density fluctuations (see eq.10). Interesting for the recording of thermo-acoustic oscillations are also acoustic cavity resonances in the liner without flame. These cavity resonances (standing pressure waves) were tested with a speaker placed 700mm above the lid with rubber layer and a pipe insulating vibrations and reducing sound emission into the laboratory. To avoid artifacts by non-uniform excitation from the speaker the cross-correlation power spectrum was recorded between laser vibrometer output and microphone output and is presented in Fig. 7 for scanning position  $x=180\text{mm}$  and  $y=0\text{mm}$ . From the frequency spectra the mode shapes for two cavity resonances are plotted. The microphone was always in position  $x=-140\text{mm}$ ,  $y=150\text{mm}$ ,  $z=150\text{mm}$  and moved together with the liner while the field was scanned.

#### 4.3 Thermo-acoustic oscillations

In Fig.8 two different flame shapes are discussed. One is for  $\phi=1.4$ , mass ratio 1.73 with an attached flame, the other one for  $\phi=1.1$ , mass ratio 0.89 shows a lifted flame. The lifted flame exhibits strong thermo-acoustic oscillations between 200 and 230 Hz when operated in the liner. In both cases the model combustor is swirl stabilized. This concept is also used in turbomachinery, eases ignition and stabilizes operation. At pre-mixed combustion a recirculation zone forms, bringing hot gas back into the flame region where it helps to ignite the fresh fuel-air mixture from the injector. This flow behavior is nicely seen in the schlieren visualization presenting the streamlines (always on the left of Figs.8a-d) and spectral emittance  $I_{430\text{nm}}$  at

430nm (CH\*) (always right). Both data sets are line-of sight data. While in the combustion zone a high level of turbulence with very small structures is observed in the time-averaged schlieren image, the swirl is identified by the curled schlieren streaks. In the recirculation area the gas is hot, the density gradients are less pronounced, and a more uniform pattern appears. The swirl and vortex breakdown drives this recirculation. The CH\* emission image helps to identified the combustion zone. When the flame was operated inside the liner (Figs.8b and d) the strongest density gradients were observed between hot flame and cold cooling flow through the perforated plate and from the settling chamber underneath the flame. Most important was a strong thermo-acoustic oscillation excited at app. 200Hz inside the liner. While such an oscillation was detected in the confined environment the combustion zone was pushed slightly towards the burner nozzle (please compare Figs8a and b).

To investigate the thermo-acoustic oscillation closer, the laser beam from the single laser vibrometer was aligned through position  $x=10\text{mm}$ ,  $y=3\text{mm}$  (line-of-sight measurement in  $z$ -direction). The first recordings were validations of setup and system sensitivity and are shown in Fig.9. These recordings were done without any flow (blue line in Fig.9) and shows only electronic noise, with suction blower and cooling air on (still no detectable signal), and with the Methane/air mixture for the lifted flame ( $\phi=1.1$ , mass ratio 0.89). This mixture was not ignited and shows the frequency behavior of a jet, peaking at about 250Hz. The recordings in Fig.9 were done without liner.

With the laser beam in the same position as in Fig.9 the Methane/air mixture was ignited. The results of these recordings are shown in Fig.10, still without liner and for three different flames conditions. The lifted flame at  $\phi=1.1$  and mass ratio 0.89 exhibited oscillations at 230 Hz in the area underneath the flame and in the combustion zone, with one second harmonic at 460 Hz, while the attached flames had a smooth spectrum. The frequency spectrum from the lifted flame at  $\phi=1.1$  and mass ratio 0.89 is shown a second time in Fig.11 for purpose of comparison (Fig.11, red line). Even without liner this ‘oscillating’ flame became temporally unstable. The otherwise lifted flame then partially attached, the oscillation frequency changed for app. 30Hz (Fig.11, green line). With liner, both frequencies can be observed underneath the flame, with the 200Hz frequency more pronounced throughout the field (Fig.11, blue line).

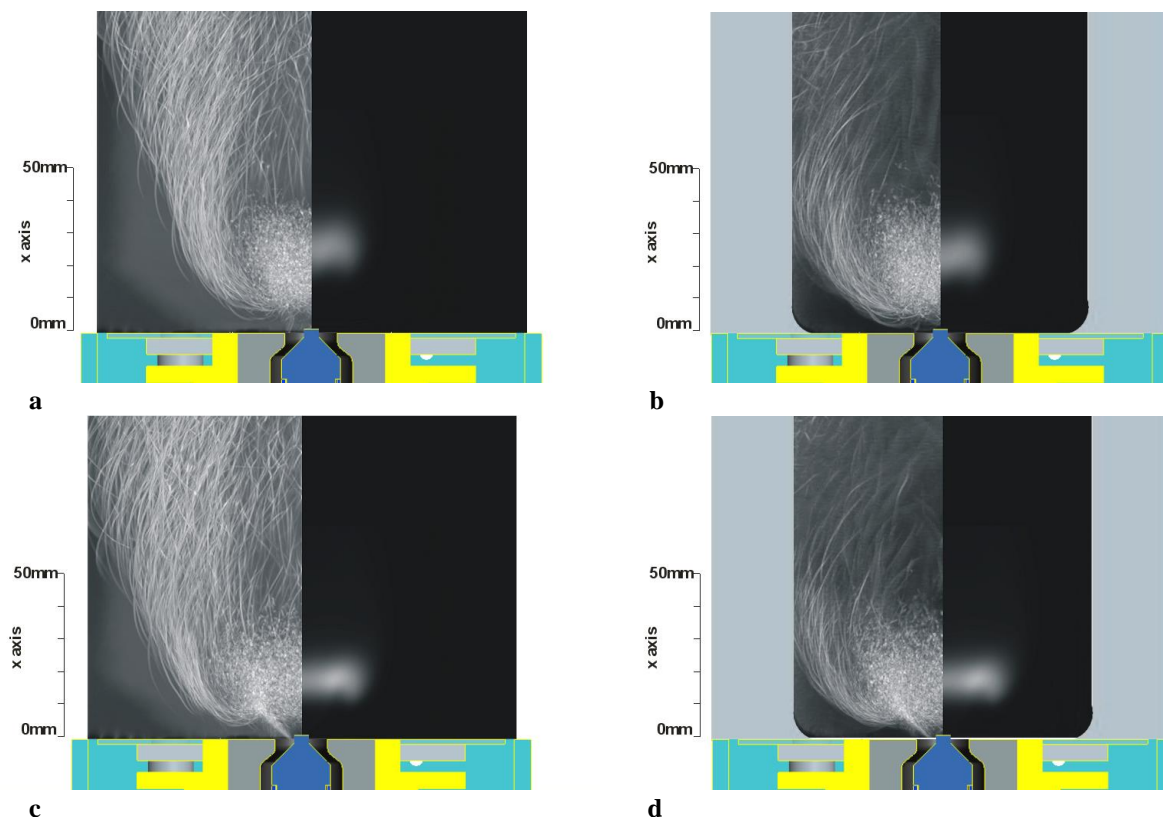


**Fig. 8** Flow and combustion visualization. In each frame, schlieren visualization (time-average on 700 recordings) is left, spectral emittance  $I_{430\text{nm}}$  at 430nm (CH\*) is right (line-of sight data). **a)**  $\phi=1.1$ , mass ratio 0.89, lifted flame, no liner. **b)**  $\phi=1.1$ , mass ratio 0.89, lifted flame, with liner, strong thermo-acoustic oscillation **c)**  $\phi=1.4$ , mass ratio 1.73, attached flame, no liner. **d)**  $\phi=1.4$ , mass ratio 1.73, attached flame, with liner.

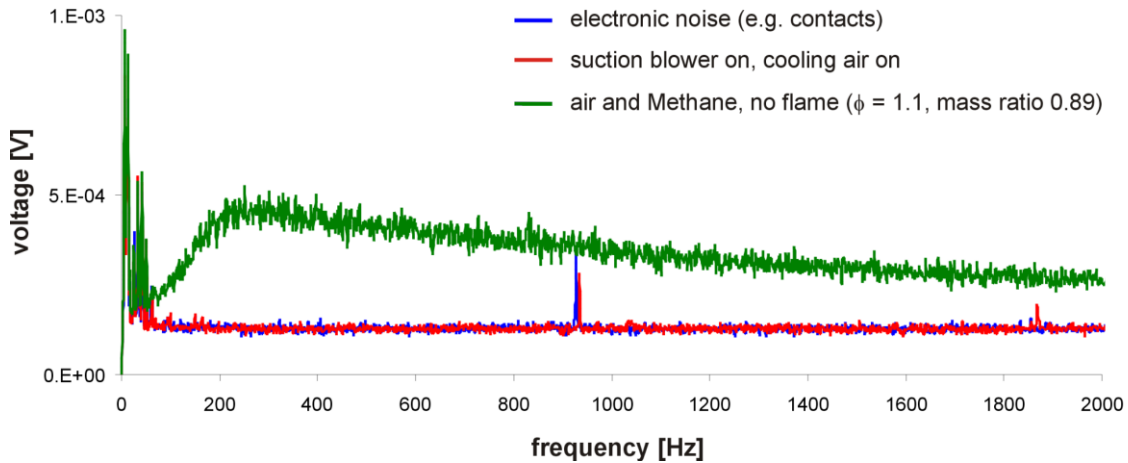


**Fig. 9** Electronic noise, background noise, and Methane/air gas flow only, not ignited ( $\Delta L=2\text{nm}$  for the Methane air mixture at 250Hz). The recordings were done without liner.

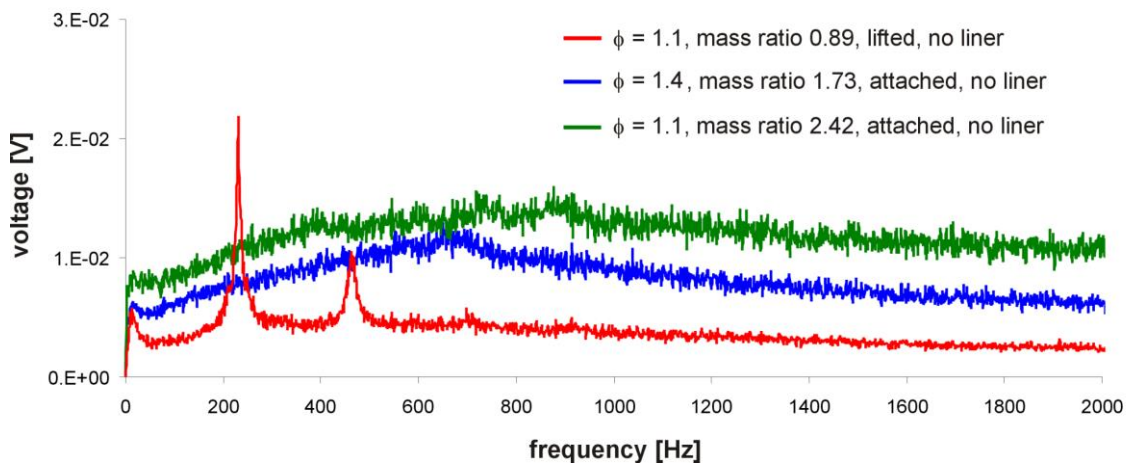


**Fig. 10** Frequency spectra of the density fluctuations at position  $x=10\text{mm}$ ,  $y=3\text{mm}$ . In this line-of-sight measurements three different flame conditions are compared, all operated without liner. The lifted flame at  $\phi=1.1$  and mass ratio 0.89 exhibits oscillations in the area underneath and in the combustion zone. For this lifted configuration  $\Delta L$  equals 98nm at resonance frequency 230Hz.

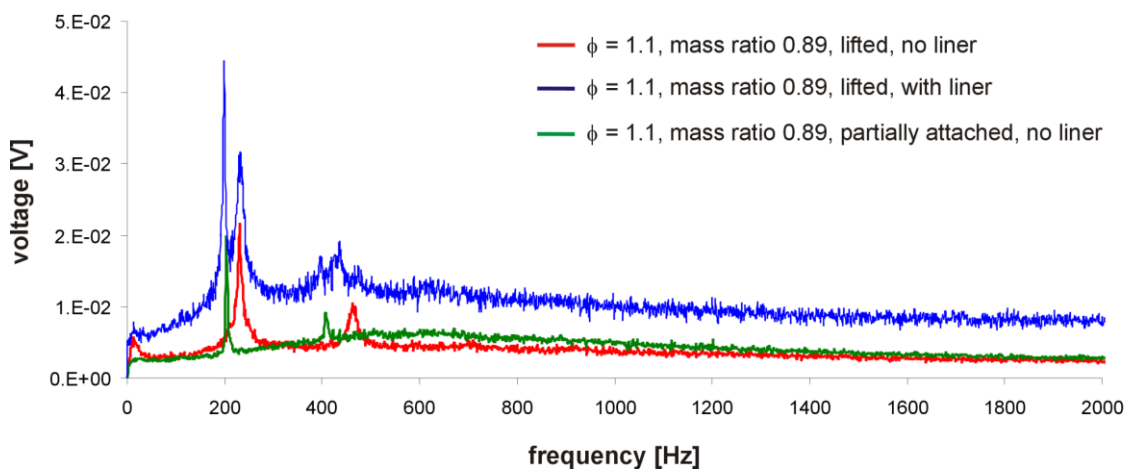


**Fig. 11** Frequency spectra of the density fluctuations at position  $x=10\text{mm}$ ,  $y=3\text{mm}$  with and without liner at the same flow conditions  $\phi=1.1$ , mass ratio 0.89. Even without liner the flame became temporally unstable. The otherwise lifted flame then partially attached, the frequency changed for app. 30Hz. ( $\Delta L=196\text{nm}$  at 200Hz with liner).

For this investigation a variable geometry premixed swirl-stabilized Methane/air burner was combined with an optically accessible liner at atmospheric pressure. In order to validate the uniformity of the equivalence ratios in the flame, OH\*/CH\* ratios were tested. This was done by recording the spectral emittance  $I$  at 310nm (OH\*) and 430nm (CH\*) for  $\phi = 1.4$  at mass ratio 1.73 (attached flame) and  $\phi = 1.1$  at mass ratio 0.89 ('resonant' flame). The results are shown in Fig.12 with unconfined and confined flame conditions compared. The first line in Fig.12 plots the emittance as recorded by the Lavisson Nanostar through the 430nm bandpass filter (line-of-sight recordings). In the second line OH\*/CH\* ratios from the Abel-inverted line-of-sight recordings are calculated. This calculation relates local spectral emittances as recorded by the Lavisson Nanostar through the narrow band filters to each other. All image intensities were corrected with respect to the filter transmissions and camera spectral response as provided by the specification sheets. For purpose of comparison the last line in Fig.12 gives the OH\*/CH\* ratios directly from the line-of-sight images recorded. Basically the OH\*/CH\* ratios must be the same whether calculated from the local data after Abel inversion or from the line-of-sight data, because the emission volume along the z-axis is always the same for 310nm or 430nm spectral emittance. For the tomographic reconstruction process (using IDEA 1.7.31 software) a convolution scheme was used with 0.54 as parameter for the Hanning window and 40 as units length parameter (which gives the sampling frequency within the projections). Using the same projection 40 times for a tomographic reconstruction is advisable in this case, since classic Abel-inversion (e.g. Backus-Gilbert method) has a tendency to add up noise in the center of the reconstructed field (Pretzler et al. 1992). The center is a region of special interest in this swirl-stabilized flame. But also the convolution scheme has drawbacks. It adds a uniform but small 'waviness' to the reconstruction which does not influence the reconstruction significantly, but might influence the following division of two small numbers. Therefore areas with too small values of spectral emittance  $I_{310nm}$  or  $I_{430nm}$  were masked in Fig.12, second line.

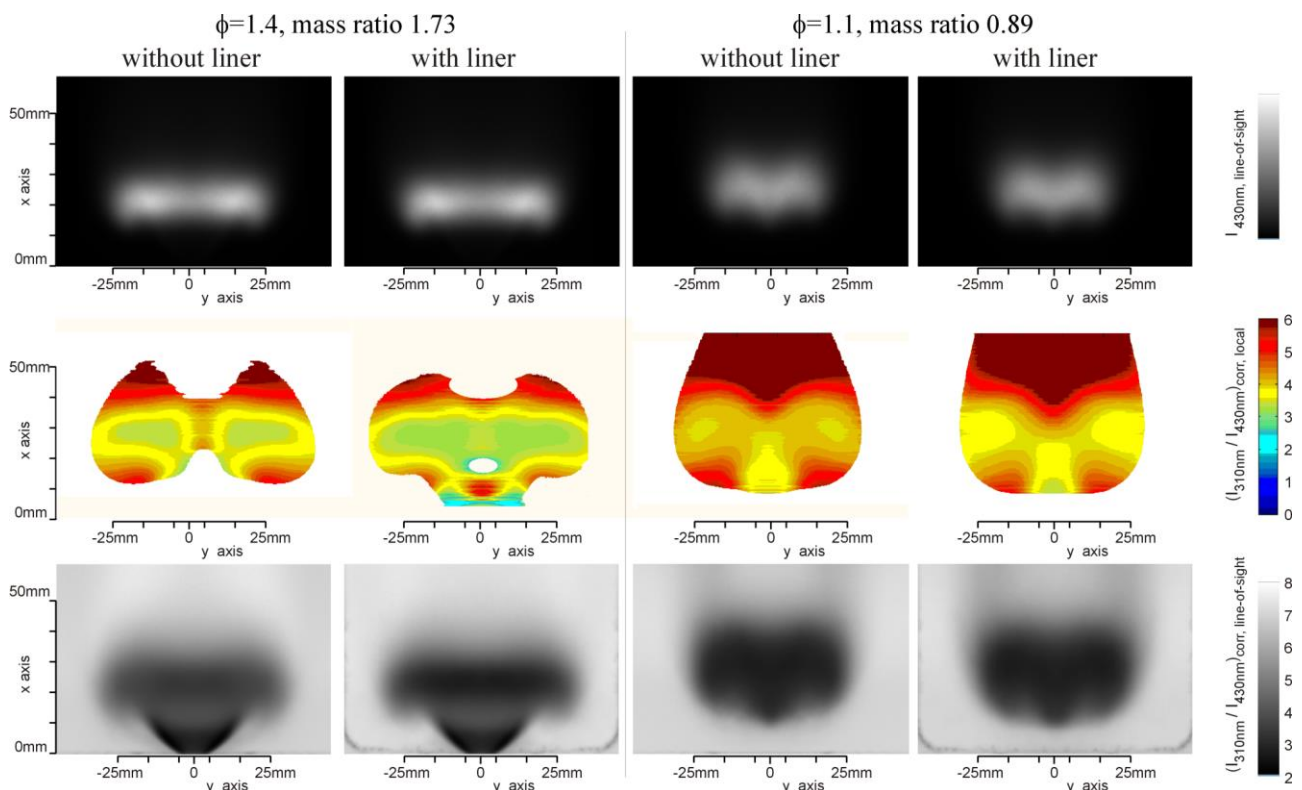


**Fig. 12** OH\*/CH\* ratios from the spectral emittance  $I$  at 310nm (OH\*) and 430nm (CH\*) for  $\phi = 1.4$  at mass ratio 1.73 (attached flame) and  $\phi = 1.1$  at mass ratio 0.89 ('resonant' flame). Compared are unconfined and confined flame conditions. The first line plots are the intensities as recorded by the Lavisson Nanostar. In the second line OH\*/CH\* ratios from the Abel-inverted line-of-sight recordings are calculated (local spectral emittances related to each other). The last line gives the OH\*/CH\* ratios directly from the line-of-sight images. All image intensities were corrected with respect to the filter transmissions and camera spectral response.

From all the results in Fig.12 it becomes evident that the lifted and resonant flame condition at  $\phi = 1.1$  at mass ratio 0.89 is nearly perfectly premixed, while the equivalence ratio in the attached flame is influenced by the cooling air to a higher degree. Comparing the  $\text{OH}^*/\text{CH}^*$  ratios from Fig.12 with characteristics given by Panoutsos et al. (2009) it turns out that the effective equivalence ratios in the combustion zone are slightly below the adjusted ones. For the  $\phi = 1.1$  flame  $\phi_{\text{effective}}$  is about 0.9, for the  $\phi = 1.4$  condition  $\phi_{\text{effective}}$  is about 1.1. No background correction from  $\text{CO}_2^*$  emission was taken into account.

To record thermo-acoustic oscillations in the flame and within the liner the laser beam from the single laser vibrometer was scanned through the field to record line-of-sight data. In a next step Abel inversion can calculate local data from these projections recorded from a rotational symmetric flame. But first the integral voltage values were transformed into integral phase-shifts (optical path differences  $\Delta L$ ) by eq.10. These data sets are presented in Figs.13 and 14 for the unconfined and the confined flame at  $\phi = 1.1$  at mass ratio 0.89.

The optical path difference and thus the density fluctuations can always be given for a single frequency or for a frequency range, but all such summations must be performed in the power spectrum and must consider the  $2\pi f$  factor. From these sums the RMS or maximum value of optical path difference  $\Delta L$  (eq.10) can be calculated with the calibration factor  $k$  resulting in a value for  $\Delta L_{195-205\text{Hz}}$  or  $\rho'_{195-205\text{Hz}}$ . Here the single frequency pin was 1Hz due to the parameters chosen for sampling frequency and sample length.

Simultaneously, a reference signal from a microphone was recorded. This microphone was fixed to the base of the burner and did not change position relative to the flame, while the burner was traversed. Thus, a permanent reference for the phase in different scanning positions was provided. As a result not only the line-of-sight optical path difference can be plotted, but also the phase of the emitted acoustic wave for different positions in space relative to the phase at the local reference.

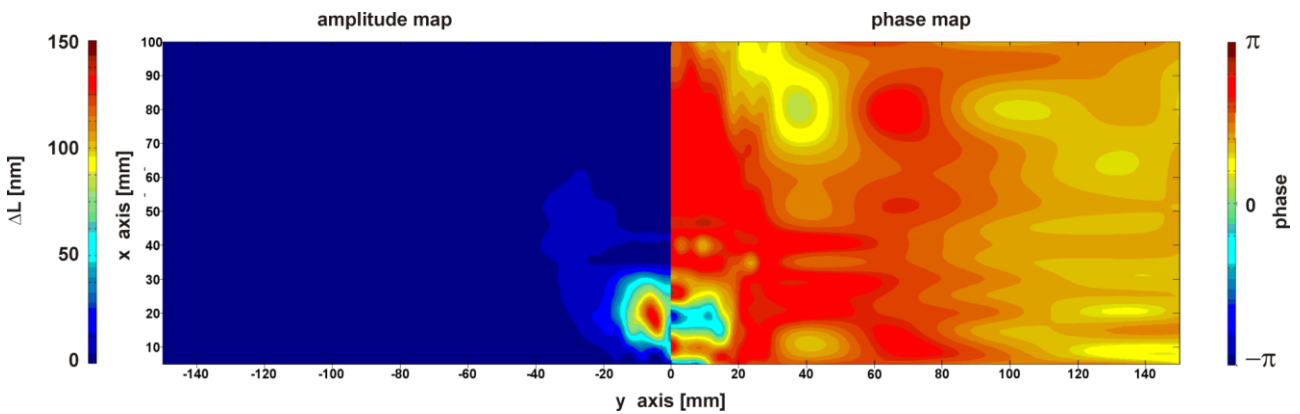


**Fig. 13** Laser vibrometer line-of-sight measurements,  $\phi=1.1$ , mass ratio 0.89, lifted, without liner ( $\Delta L$  for 200-250Hz range). The left side represents the optical path difference (amplitude), while the right side gives the phase map indicating the sound propagation from the thermo-acoustic oscillation.

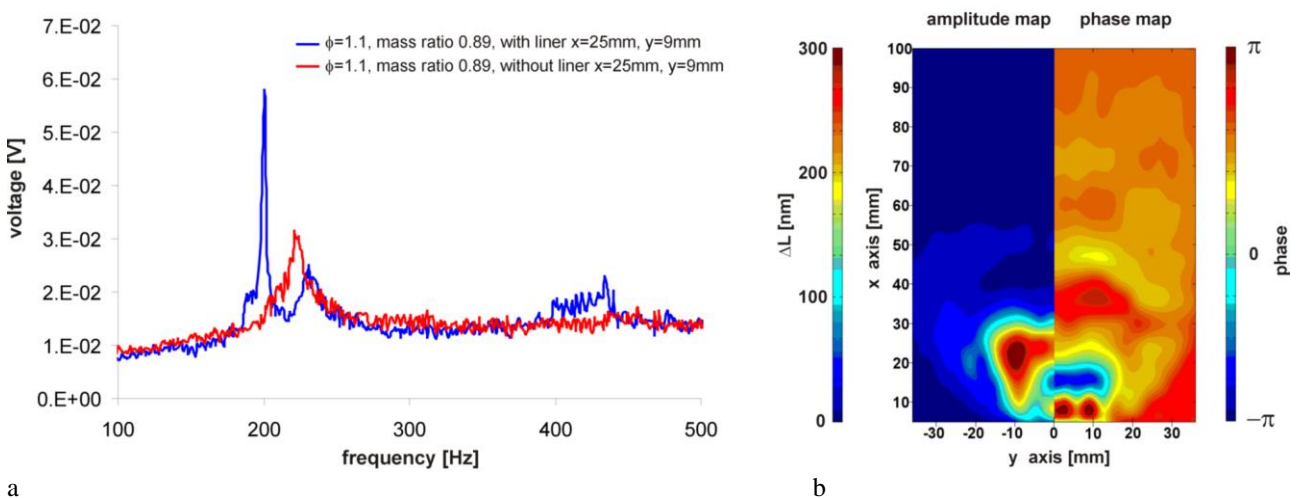


**Fig. 14** Laser vibrometer line-of-sight measurements, **a)**  $\phi=1.1$ , mass ratio 0.89, lifted, with and without liner. **b)**  $\phi=1.1$ , mass ratio 0.89, lifted, with liner ( $\rho'$  for 195-205 Hz range)

The  $\Delta L$  maps in Figs.13 and 14 indicate that the strongest density fluctuations occur underneath or in the flame. Especially when operated in the liner (Fig.14b) the flame has a strong tendency to periodically snap towards the burner. During this process the resonance frequency slightly changes. This change is shown in Fig.14a with the unconfined flame having a thermo-acoustic resonance closer to 230Hz. In the confined environment the flame starts to oscillate at a slightly lower frequency slightly above 200Hz. Even in the spectral emittance plots it can be seen that the flame is now closer to the burner influencing this resonance frequency. In any case cavity resonances can be excited at these frequencies.

From the phase plots it is seen that there is a phase lag between flame oscillations and pressure wave. From Rayleigh criterion - which related pressure fluctuations with heat release - it is known that the acoustic energy tends to increase when pressure and heat release have a component that is in phase (between  $-\pi/2$  and  $\pi/2$ ; see Dowling and Morgans, 2005). In a flame and under atmospheric conditions the heat release term surpasses the pressure term, while outside the flame the heat release contribution can be neglected (eq.1). When scanning the phase maps a phase lag between the density fluctuations from within the flame and from outside the combustion zone can be observed, depending on whether a thermo-acoustic oscillation is excited at this frequency or not. While the unconfined flame emits an acoustic pressure wave mainly horizontally, the confined flame excites a cavity resonance in axial direction.

## 5. New grounds: Discussing local data recording and structural decay

### 5.1. Dual laser vibrometry

In the last section we tested the flow for thermo-acoustic oscillations and used line-of-sight measurements only. From the vibrometer output (in Volt) we calculated optical path changes for single frequencies or frequency bands using eq.10. These optical path changes are caused by a change in refractive index which is related to the density by eqs. 2a and b. Such integral scans at  $x=25\text{mm}$  are shown in Fig.15 for  $\phi=1.4$  at mass ratio 1.73 (attached flame, Fig.15a blue line) and  $\phi=1.1$  at mass ratio 0.89 ('resonant' flame, Fig.15b blue line). Assuming a constant index distribution over the estimated flame diameter (here  $\Delta z=35\text{mm}$ ), the average density fluctuation in the frequency range chosen can be estimated. This value only gives the order of magnitude for the density fluctuations to be expected but serves as reference to verify the results from tomography reconstruction or dual laser vibrometry. To obtain a more accurate information on local data from line-of-sight measurements a tomographic reconstruction is needed. 21 positions with 3mm distance in radial direction at  $x=25\text{mm}$  were sampled with the flame operated under confined conditions in the liner. Due to the rotational symmetry and due to the small number of positions sampled we applied an Abel inversion - a Backus-Gilbert scheme turned out to be best. (In software IDEA the local data can be integrated again so that a quality check between reconstructed field and the original projection data is possible).

For tomographic reconstructions the data set must be zero in the two outermost positions, otherwise a tomographic reconstruction is not possible. This was not the case for the  $\phi=1.1$ , mass ratio 0.89 flame which exhibits strong thermo-acoustic oscillations. Therefore a zero-line shift was performed, assuming that this offset is uniform throughout the  $140 \times 140\text{mm}^2$  liner. Under such an assumption of uniformity a local density fluctuation was calculated and afterwards added to the result from the Abel inversion. In Fig.15b this result is shown as 'local data from Abel inversion, with offset correction' (Fig.15b, green line). For the non-resonant attached flame at  $\phi=1.4$  and mass ratio 1.73 the inversion was straight-forward, the projection data were zero at the boundaries.

After inversion to local data the density fluctuations obtained from the Abel inversion can be assumed constant over the pixel size within the reconstructed tomographic cross-section of  $n \times n \text{ pixel}^2$  with  $n$  the number of pixel in the projection. Now, the integral in eq.2a becomes a multiplication with the pixel length in  $z$  direction (3mm in Fig.15) allowing the calculation of the local fluctuations in refractive index for the frequencies tested. Finally the Gladstone-Dale constant for the gas is needed to calculate density fluctuations from fluctuations in refractive index. Köberl et al. (2010) recorded the concentrations of gas components in the combustion zone of a Methane/air flame with Raman spectroscopy. It turns out that especially for Oxygen, Carbon Dioxide and air the Gladstone Dale constants do not differ much from each other (Gardiner et al. 1981), while the value for Methane is 2.4 times higher compared to that of air. Therefore we used the equivalence ratios from Fig.12 to calculate the correct Gladstone-Dale constant for our gas in the combustion zone which resulted in a value of  $G=2.61 \cdot 10^{-4} \text{ kg/m}^3$  for the Gladstone-Dale constant.

Often, local densities are needed from non-axis-symmetric flames or from a confined environments. Limited optical access often renders multidirectional observation for a tomographic reconstruction impossible. Then

a dual laser vibrometry can be used and signals from two laser vibrometers can be correlated to record local data (Hampel et al. 2006). For this technique two vibrometers are positioned orthogonal to each other, forming an interrogation area in the flow where the beams intersect. The evaluation and validation was performed according to eqs.7-9 with a high number of samples needed in order to obtain a good signal-to-noise ratio even in highly turbulent flows or combustion. Such a recording was done for the attached flame ( $\phi=1.4$ , mass ratio 1.73) and for the lifted flame ( $\phi=1.1$ , mass ratio 0.89, with thermo-acoustic oscillations) at height  $x=25\text{mm}$ , both operated in the liner under confined conditions. The result is shown in Fig.12, first without phase filter (brown line in Fig.15), then with a phase filter  $\Delta\Phi=1\text{rad}$  (red line).

In jets the vortex shedding from different positions in the nozzle is generally correlated due to conservation of angular momentum (Hampel et al., 2006), but the phase lag between the shedding vortices usually differs from zero along the circumference. Without phase filter these contributions will add up in the center and the rim of the local distributions when recorded by dual laser vibrometry (brown lines in Fig.15). When a phase filter  $\Delta\Phi=1\text{rad}$  was applied to the data recorded by dual laser vibrometry, the density fluctuations recorded in radial direction through the center of the flame resulted in the same distribution compared to the Abel inversion calculated from the integral line-of-sight measurements done with one laser. But only for the  $\phi=1.4$ , mass ratio 1.73 conditions outside thermo-acoustic resonance (Fig.15a, red and green lines).

The situation is completely different for the confined  $\phi=1.1$ , mass ratio 0.89 flame at resonance frequency. Here the thermo-acoustic oscillations in the liner bring all fluctuations at resonance frequency in phase. For this frequency the application of the phase filter to data recorded by dual laser vibrometry improves the result only slightly. So, this technique of dual-laser vibrometry is not suitable for the detection of local density fluctuations at resonance frequencies (Fig.15b red line).

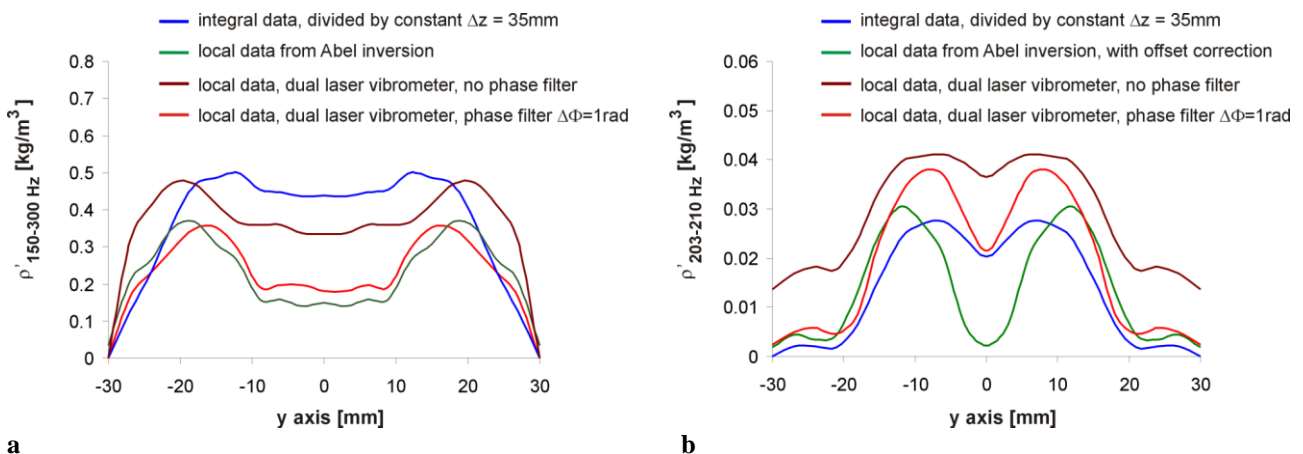


**Fig. 15** Local density fluctuations: laser vibrometer line-of-sight measurements at  $x=25\text{mm}$ . **a)**  $\phi=1.4$ , mass ratio 1.73, lifted, with and without liner ( $\rho'$  for 150-300 Hz range). **b)**  $\phi=1.1$ , mass ratio 0.89, lifted, resonant, with liner ( $\rho'$  for 195-205 Hz range).

## 5.2. Structural decay and velocity

In section 5.1 two laser vibrometers were used to correlate signals from density fluctuations to record local data in the interrogation area formed by the two intersecting laser beams (Fig.16a). Either one, or both vibrometers can be traversed horizontally, or the burner is traversed in order to get radial profiles of density fluctuations at certain frequencies or frequency bands with the vibrometers fixed. This dual vibrometer technique was discussed in section 5.1.

A second possibility is to scan the flow in axial direction with only one laser vibrometer, while the second vibrometer and the burner are fixed. When a density fluctuation now firstly crosses laser beam 1, secondly beam 2, a phase delay is recorded, depending on the velocity of this structure in axial direction. Whenever such a structure decays while moving in axial direction, or leaves the test volume due to tangential motion, the correlation will be lost.

Such a scan for density fluctuations at frequencies between 0 and 300Hz is shown in Fig.17a. Scanning direction was in axial flow direction, starting position was  $x=60\text{mm}$ ,  $y=10\text{mm}$ ,  $z=-10\text{mm}$ . At low frequencies below 50Hz vibrations and noise is seen in Fig.17a. At about 200Hz the field is dominated by the thermo-acoustic oscillations. Due to the high speed of sound no significant phase shift is observed for the scanning

length of 27mm (in 3mm steps). The position of the  $2\pi$ - jumps in phase is also indicated in Fig.17a by a dashed line. From the phase delays plotted in Fig.17b for 150Hz and 240Hz the axial velocity can be estimated from

$$u = \Lambda f \quad , \quad (11)$$

with  $u$  the mean axial velocity,  $\Lambda$  the structure size and  $f$  the frequency. From Fig.17b we learn that at 160Hz the phase delay is close to  $4\pi$  (with one mod  $2\pi$  phase step), meaning two periods of  $\Lambda_{160\text{Hz}}$  within 27mm or  $\Lambda_{150\text{Hz}}=13.5\text{mm}$ . Together with eq.11 we then get  $u = 2.2\text{m/s}$ , which is in accordance with the PIV measurements done by Giuliani et al. (2012). At 230Hz the  $4\pi$  phase delay is detected after 20mm, resulting in  $u = 2.3\text{m/s}$  axial velocity.

Additional information is given by the degree of correlation calculated from the correlation amplitude spectrum related to the amplitudes of the single laser vibrometer spectra. Within the last two positions scanned at 230Hz, this value decreased by a factor of 5-10 indicating a loss of coherence. This loss of coherence might be due to a decay of these 10mm structures within 20 to 30mm. This loss of coherence might also be caused by strong radial or tangential movement, due to the swirl of the flame. Here, one might think of using a laser sheet rather than a beam to detect such structures and their decay more easily.

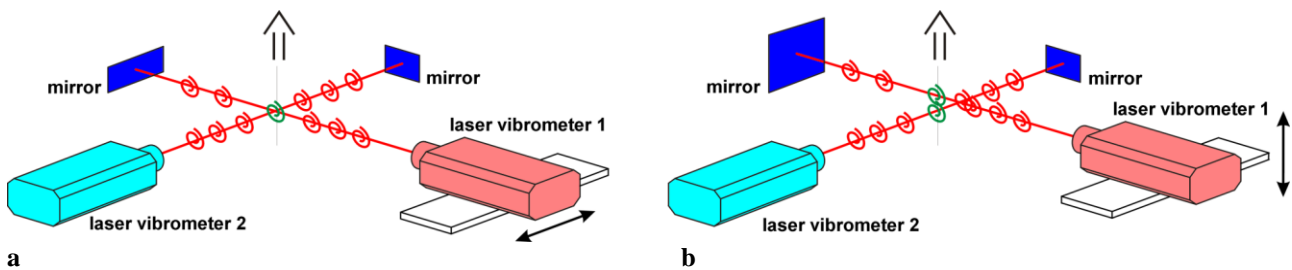


**Fig. 16 a)** setup for dual laser vibrometry to record local density fluctuations interferometrically. Either one laser vibrometer scans the flow, or the burner is traversed. The scan is horizontally. Only fluctuations shown in green should correlate within a in given phase lag  $\Delta\Phi$  in order to obtain local information. **b)** One of the two laser vibrometers is traversed vertically to record the phase delay of structures firstly passing through beam 1, then through beam 2. Structural velocities and decay can be estimated from the phase delays recorded at different frequencies.

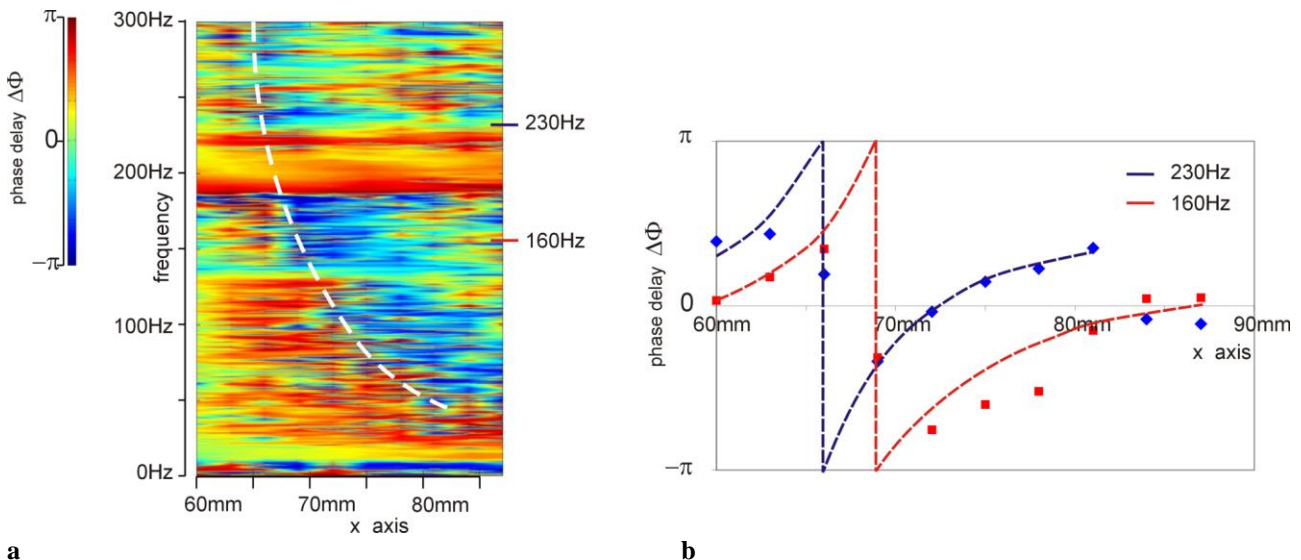


**Fig. 17 a)** Phase delay between density fluctuation firstly crossing laser beam 1, then beam 2 for frequencies between 0Hz and 300Hz. Scanning direction is in axial flow direction, starting position was  $x=60\text{mm}$ ,  $y=10\text{mm}$ ,  $z=-10\text{mm}$ . At low frequencies below 50Hz vibrations and noise is seen. At about 200Hz the field is dominated by the thermo-acoustic oscillation. Due to the high speed of sound no significant phase shift is observed for the scanning length of 27mm (in 3mm steps). **b)** Estimation of axial velocity from phase delay at two frequencies ( $u=2\text{m/s}$ ). The position of the mod  $2\pi$  phase steps are indicated in a) by a dashed line.

## Acknowledgements

This research was funded by the Austrian Science Fund FWF within grant FWF-24096-N24 “Interferometric Detection of Thermoacoustic Oscillations in Flames”. The authors would like to thank Dr. Andreas Marn for his kind support and the ongoing discussion on acoustics.

## References

- Buick JM, Cosgrove JA, Douissard PA, Greated CA, Gilibert B (2004) Application of the acousto-optic effect to pressure measurements in ultrasound fields in water using a laser vibrometer, *Rev. Sci. Instrum.* 75:3203–3207
- Dowling AP, (1995) The calculation of thermoacoustic oscillations. *Journal of Sound and Vibration* 180: 557-581
- Dowling AP, Morgans AS (2005) Feedback control of combustion oscillations. *Annual Review of Fluid Mechanics* 37:151-182.
- Fischer A, König J, Czarske J, Peterleithner J, Woisetschläger J., Leitgeb T. (2013) Analysis of flow and density oscillations in a swirl-stabilized flame employing highly resolving optical measurement techniques, *Experiments in Fluids* 54:1622 (18pp)
- Floyd J, Kempf AM (2011) Computed Tomography of Chemiluminescence (CTC): High resolution and instantaneous 3-D measurements of a Matrix burner, *Proceedings of the Combustion Institute* 33:751–758
- Gardiner WC, Hidaka Y Jr., Tanzawa T (1981) Refractivity of combustion gases, *Combustion and Flame* 40:213-219
- Giuliani F, Leitgeb T, Lang A, Woisetschläger J (2010) Mapping the density fluctuations in a pulsed air-methane flame using laservibrometry. *J Eng Gas Turbines Power* 132:0316031 (p 8)
- Giuliani F, Woisetschläger J, Leitgeb T (2012) Design and validation of a burner with variable geometry for extended combustion range, *Proceedings of ASME Turbo Expo 2012, GT2012*, June 11-15, 2012, Copenhagen, Denmark, GT2012-68236
- Gren P, Tatar K, Granström J, Molin N-E, Jansson E V (2006) Laser vibrometry measurements of vibration and sound fields of a bowed violin *Meas. Sci. Technol.* 17:635–44
- Guyot D, Guethe F, Schuermans B, Lacarelle A, Paschereit CO (2010) CH\*/OH\* chemiluminescence response of an atmospheric premixed flame under varying operating conditions, *Proceedings of ASME Turbo Expo 2010:GT2010-23135*
- Hampel B, Woisetschläger J (2006) Frequency- and space-resolved measurement of local density fluctuations in air by laser vibrometry, *Meas. Sci. Technol.* 17:2835–42.
- Harland AR, Petzing JN, Tyrer JR (2007) Visualising scattering underwater acoustic fields using laser Doppler vibrometry, *J. Sound & Vibration* 305:659–671
- Harland AR, Petzing JN, Tyrer JR, Bickley CJ, Robinson SP, Preston RC (2003) Application and assessment of laser Doppler velocimetry for underwater acoustic measurements, *J. Sound & Vibration* 265:627–645
- Hardalupas Y, Orain M (2004) Local Measurements of the Time-dependent Heat Release Rate and Equivalence Ratio Using Chemiluminescent Emission from a Flame. *Combustion and Flame* 139:188–207
- Hardalupas Y, Panoutsos CS, Taylor AMKP (2010) Spatial resolution of a chemiluminescence sensor for local heat-release rate and equivalence ratio measurements in a model gas turbine combustor, *Exp Fluids* 49: 883–909
- Hipp M, Reiterer P, Woisetschläger J, Philipp H, Pretzler G, Fliesser W, Neger T (1999) Application of interferometric fringe evaluation software at Technical University Graz, *Proc. SPIE* 3745 281–92
- Hipp M, Woisetschläger J, Reiterer P, Neger T (1999) Digital evaluation of interferograms, *Measurement* 36:53–66
- Köberl S, Fontaneto F, Giuliani F, Woisetschläger J (2010) Frequency resolved interferometric measurement of local density fluctuations for turbulent combustion analysis, *Meas. Sci. Technol.* 21:035302 (10pp)
- Lauer M, Sattelmayer T (2010) On the adequacy of chemiluminescence as a measure for heat release in turbulent flames with mixture gradients, *J. Eng. Gas Turbines and Power* 132: 061502 (8pp)
- Lechner C, Seume J (2010) *Stationäre Gasturbinen*. Springer, Berlin Heidelberg New York, pp. 1100.
- Leibovich S (1978) The structure of vortex breakdown. *Annu Rev Fluid Mech* 10:221–246
- Leitgeb T, Schuller T, Durox D, Giuliani F, Köberl S, Woisetschläger J. (2013) Interferometric determination of heat release rate in a pulsated flame, *Combustion and Flame* 160:589–600

- Lewin A (1999) New compact laser vibrometer for industrial and medical applications 3rd Int. Conf. on Vibration Measurements by Laser Techniques, ed E P Tomasini, SPIE Proc. Series 3411:61–7
- Lieuwen, TC, Yang, V (2005) Combustion Instabilities in Gas Turbine Engines - Operational Experience, Fundamental Mechanisms, and Modeling. Progress in Astronautics and Aeronautics, American Institute of Aeronautics and Astronautics 210
- Martarelli M, Castellini P, Tomasini EP (2013) Subsonic jet pressure fluctuation characterization by tomographic laser interferometry, Exp Fluids 54:1626
- Mayrhofer N, Lang H, Woisetschläger J (2000) Experimental investigation of turbine wake flow by interferometrically triggered LDV-measurements, Proc.10th Int. Symp. on Application of Laser Techniques to Fluid Mechanics (Instituto Superior Tecnico, Lisboa), paper 28-1
- Mayrhofer N, Woisetschläger J (2001) Frequency analysis of turbulent compressible flows by laser vibrometry Exp. Fluids 21:153–61
- Nori VN, Seitzman JM (2009) CH\* chemiluminescence modeling for combustion diagnostics, Proceedings of the Combustion Institute, 32:895-903
- Panoutsos CS., Hardalupas Y, Taylor AMKP (2009) Numerical evaluation of equivalence ratio measurement using OH\* and CH\* chemiluminescence in premixed and non-premixed methane–air flames, Combustion and Flame 156:273–291
- Peterleithner JJ, Marn A, Leitgeb T, Woisetschläger J (2013) Frequency Resolved Density Fluctuation Measurements of Combustion Oscillations in a Model Combustor, 49th AIAA/ASME/SAE/ASEE Joint Propulsion Conference & Exhibit, 15 - 17 Jul 2013, San Jose, CA , Paper No.: 1589261
- Pretzler G, Jäger H, Neger T, Philipp H, Woisetschläger J (1992) Comparison of different methods of Abel inversion using computer simulated and experimental side-on data, Z. Naturforsch. 47a:955-970
- Settles GS (2006) Schlieren & Shadowgraph Techniques, 2nd edition, Springer, Wien Heidelberg New York
- Wang S, Hsieh SY, Yang V (2005) Unsteady flow evolution in swirlinjector with radial entry. I. Stationary conditions. Phys Fluids 17:045106 (p 13)
- Woisetschläger J, Lang H, Hampel B, Göttlich E, Heitmeir F (2003a) Influence of blade passing on the stator wake in a transonic turbine stage investigated by particle image velocimetry and laser vibrometry Proc. Inst. Mech. Eng. A 217:385–91
- Woisetschläger J, Mayerhofer N, Hampel B, Lang H, Sanz W (2003b) Laser-optical investigation of turbine wake flow Exp. Fluids 34:371–8
- Zipser L, Franke HH (2008) Refracto-vibrometry – a novel method for visualizing sound waves in transparent media, Acoustics'08, Paris 29 June – 4 July 2008
- Zipser L, Lindner S, Behrendt R (2002) Interferometrische Messung und Visualisierung von Schallwellen und Turbulenzen, Tech. Mess. 6: 275–81